Effect of Tool Speed on Microstructure Evolution and Mechanical Properties of Friction Stir Welded Joints of Al-Mg-Si Alloy with High Cu Content

Wangzhen Li [1,2,3], Zhang Luo [1], Youping Sun [1,2,3,*] and Xinyu Liu [1]

1   School of Mechanical and Automotive Engineering, Guangxi University of Science and Technology, Liuzhou 545006, China; liwangzhen@gxust.edu.cn (W.L.)
2   Guangxi Key Laboratory of Automobile Components and Vehicle Technology, Liuzhou 545006, China
3   Guangxi Earthmoving Machinery Collaborative Innovation Center, Liuzhou 545006, China
*   Correspondence: syptaiji@126.com

Abstract: OM, SEM, EBSD, and other analytical techniques were utilized to investigate the effects of the rotating speed of a mixing head on the microstructures and mechanical properties of a joint. The results indicate that, compared with the base material, the grain size in the nugget zone is significantly refined. Furthermore, as the rotational speed of the mixing head increases, the grain size in the nugget zone increases noticeably, and the proportion of high-angle grain boundary length initially decreases and then increases. The texture types in different areas of the joint are markedly distinct: the base material primarily consists of recrystallization texture and rolling texture, while the core zone mainly comprises C-shear texture. Among the joints tested at various rotation speeds, the lowest hardness values are observed in the advancing side heat-affected zone, and the tensile properties of the joints are notably reduced due to the dissolution and coarsening of the second phase. The joint exhibits optimal performance at 1000 r/min, with a tensile strength and elongation of 196.3 MPa and 13.5%, respectively.

Keywords: aluminum alloy; EBSD; texture; mechanical property

1. Introduction

As heat-treatable aluminum alloys, 6-series aluminum alloys possess characteristics such as low density, high specific strength, good corrosion resistance, and weldability. These attributes make them widely used across various fields, including aviation, automobiles, and shipbuilding [1]. Friction Stir Welding (FSW) is a solid-state welding process that successfully eliminates the defects associated with traditional methods. It boasts advantages such as energy efficiency, environmental protection, and high-quality connections, thereby being considered a revolutionary welding technology [2,3]. During the FSW process, friction between the tool and the workpiece generates a significant amount of heat, softening the material. Strong plastic deformation occurs under the agitation of the stirring needle, resulting in the formation of fine recrystallized grains [4,5]. The different thermal coupling effects in various areas of the joint lead to an uneven microstructural distribution, and the formation of different grains and textures directly impacts the overall performance of the welded joint. Therefore, it is crucial to study the microstructures, textural evolution characteristics, and mechanical properties of welded joints under different welding process parameters.

For FSW, tool speed, welding speed, tool shape, and other process variables greatly impact the flow and thermal cycling characteristics of materials, leading to various changes in microstructure, texture, and mechanical properties [6]. In the past, some scholars have investigated the effects of welding conditions on the microstructures and mechanical properties of aluminum alloy joints. Dong et al. [7] examined the effect of welding speed

on the microstructure and hardness of 6005A-T6 aluminum alloy, finding that the original β″ phase in the nugget zone (NZ) is completely integrated into the α-Al matrix. Moreover, a lower welding speed promotes the formation of a GP zone, thereby increasing the hardness of the welding core zone. The welding speed has little effect on the hardness of the thermos-mechanically affected zone (TMAZ), with the evolution of the precipitated phase being mainly related to the peak temperature. The heat-affected zone (HAZ) has the lowest hardness due to the coarsening of the β″ and Q′ phases, but its hardness gradually increases with increasing welding speed. Krasnowski et al. [8] studied the effects of tool shape on the microstructure and mechanical properties of 6082 aluminum alloy, discovering that the joint can achieve good tensile properties with conventional tools; however, when a non-threaded plain needle mixing head is used, the joint performance is poor. Sato et al. [9] investigated the relationship between the microstructures and microhardness of 6063 aluminum alloy joints in relation to tool speed. The researchers concluded that the change in hardness is independent of grain size, and the softening of the joint is due to the coarsening and dissolution of the β″ phase. Additionally, increasing tool rotation speed widens the softening zone of the joint. Ahmad et al. [10] explored the effects of stirring head rotation speed on the mechanical and flexural properties of 6061 aluminum alloy joints. Their research showed that the HAZ range increases with higher stirring head rotation speeds, and both hardness and flexural properties are improved.

The Cu content of 6-series aluminum alloys is generally lower than 0.4%, but it has been shown that an increase in Cu content can reduce the precipitation activation energy of the alloy [11], alter the precipitation sequence of the alloy, and improve its strength [12]. However, no one has studied the effect of higher Cu content on the FSW joints of Al-Mg-Si alloys. Therefore, in this work, the effect of rotational speed on the microstructure and mechanical properties of FSW joints of Al-Mg-Si alloys containing 0.8% Cu was investigated, providing a theoretical basis for practical applications.

2. Experimental Materials and Methods

The material used in the experiment was an Al-0.75Mg-0.75Si-0.8Cu alloy ingot, which was obtained by melting pure aluminum, pure magnesium, 10% aluminum–silicon, and 10% aluminum–copper intermediate alloys in specific proportions. The specimen size was 150 mm × 120 mm × 20 mm. Subsequently, the ingot underwent homogenization treatment at 560 °C for 24 h, after which it was processed into a 100 mm × 80 mm × 14 mm plate by milling. The plates were first rolled to 2 mm through two hot rolling steps (the first pass was 4 mm and the second pass was 8 mm) with a rolling temperature of 400 °C and a holding time of 20 min for each pass. The rolling rate was 10 s^{-1} for both passes. Finally, the plates were subjected to a solution treatment at 510 °C for 80 min and an aging treatment at 195 °C for 13 h [13].

Before welding, all plates were sanded with sandpaper and alcohol to remove the oxidized layer and grease. The diameter of the tool shoulder used for welding was 12 mm, the length of the tool pin was 1.85 mm, and its shape was conical. The large diameter of the tool pin was 3.6 mm, while the small diameter was 2.5 mm. The welding direction (WD) was perpendicular to the rolling direction (RD). An ETM105D electronic universal testing joint (Wance, made in China) was used for mechanical property testing at room temperature (tensile rate of 2 mm/min), and each group of tensile specimens was tested three times to determine the average value. A SIGMA scanning electron microscope was used to observe the fracture morphologies of the welded joints. In the welded joints, cross-section (ND) samples were used for grinding and polishing. A mixture of 70% nitric acid and 30% methanol was used for electrochemical polishing. The polishing voltage was 15 V, the polishing solution was cooled by liquid nitrogen at −35 °C, and the polishing time was 40 s. EBSD experiments were carried out using a field emission scanning electron microscope (SIGMA, Carl Zeiss, Oberkochen, Germany) with an EBSD probe (Aztec-Max80). The microhardness profile was measured in the cross-section perpendicular to the welding

direction along the mid-thickness direction of the plate using an HVS-1000A hardness tester under a 200 g load for 10 s.

3. Experimental Results and Analysis

3.1. Microstructure Analysis of Joint

Figures 1–4 illustrate the microstructural morphologies of different regions of the weld cross-section under various rotational speeds. According to Figures 1b and 2b, the NZ grains undergo dynamic recrystallization at high temperatures with strong plastic deformation; thus, the grains are very fine. However, in Figures 3b and 4b, the NZ grains obviously grow due to the increase in heat input with increasing rotational speed. The grains in the TMAZ are subjected to shear extrusion of the grains in the NZ, resulting in the presence of a clearly oriented distribution of the AS-TMAZ. This distribution leads to the appearance of a clear boundary between the HAZ of the joint and the NZ on the forward side, as shown in Figures 1a and 2a. As the rotational speed increases, the effects of temperature and shear on the TMAZ of the joint increase, and the degree of dynamic recrystallization of the grains increases. Conversely, the recrystallized grains in the NZ grow with increasing rotational speed, resulting in blurring of the boundary between the NZ and the TMAZ of the joint, as shown in Figures 3a and 4a. Similarly, the changes in the HAZ of the engine on the backward side are basically consistent with the previous analysis. However, it is interesting to note that when the rotational speed is 750 r/min, the zone of influence of the heat engine expands to the inside of the NZ on the backward side (shown by the arrows in Figure 1c). After the rotational speed is increased, the phenomenon of expanding the zone of influence of the heat engine to the inside of the NZ disappears. A reasonable explanation for this phenomenon is that the material in the upper part moves downward during the FSW process, and part of the material in the forward side accumulates in the backward side under the shearing effect of the stirring head. At low rotational speeds, the heat input is low, the material is less mobile, and less recrystallization occurs. As a result, the material accumulated on the backward side is subjected to a very strong squeezing action, leading to grain expansion in the TMAZ toward the NZ [14].
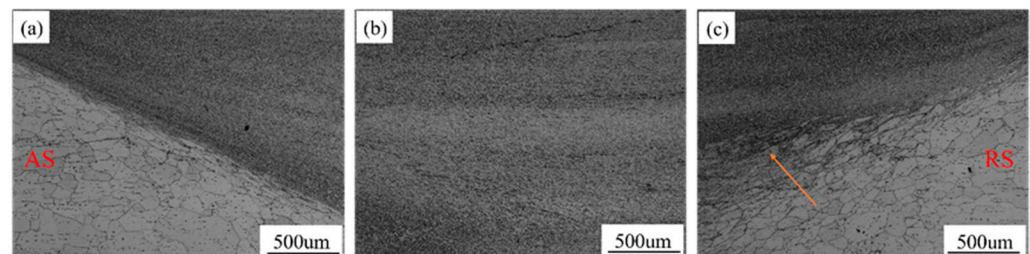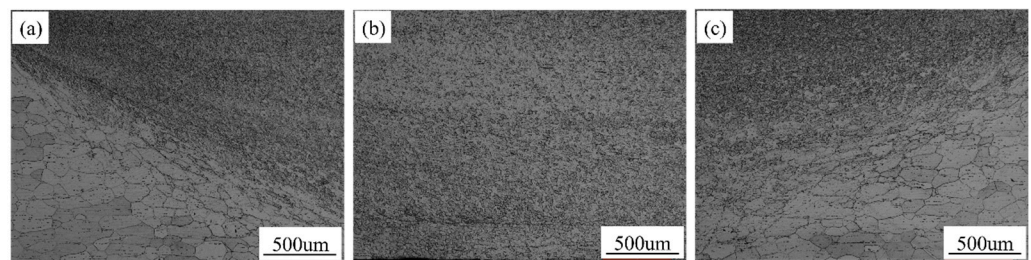

Figure 1. Microstructure of alloy FSW joint at rotation speed of 750 r/min (**a**) AS, (**b**) NZ, (**c**) RS.
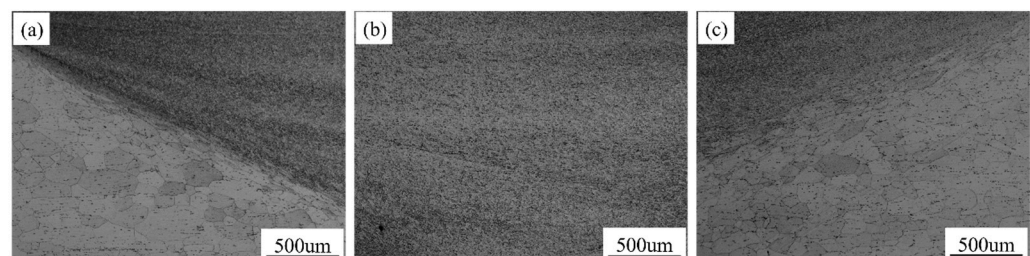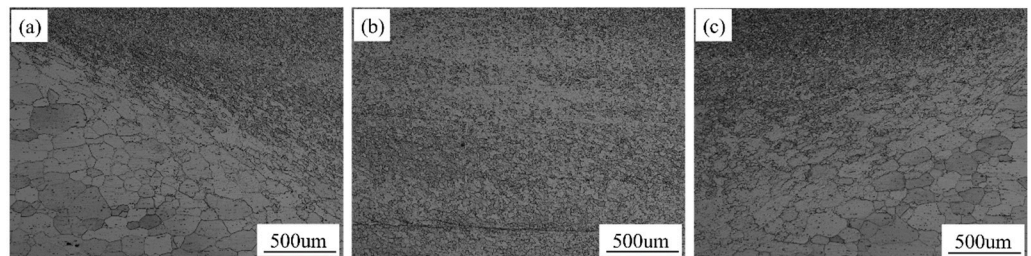

Figure 2. Microstructure of alloy FSW joint at rotation speed of 1000 r/min (**a**) AS, (**b**) NZ, (**c**) RS.
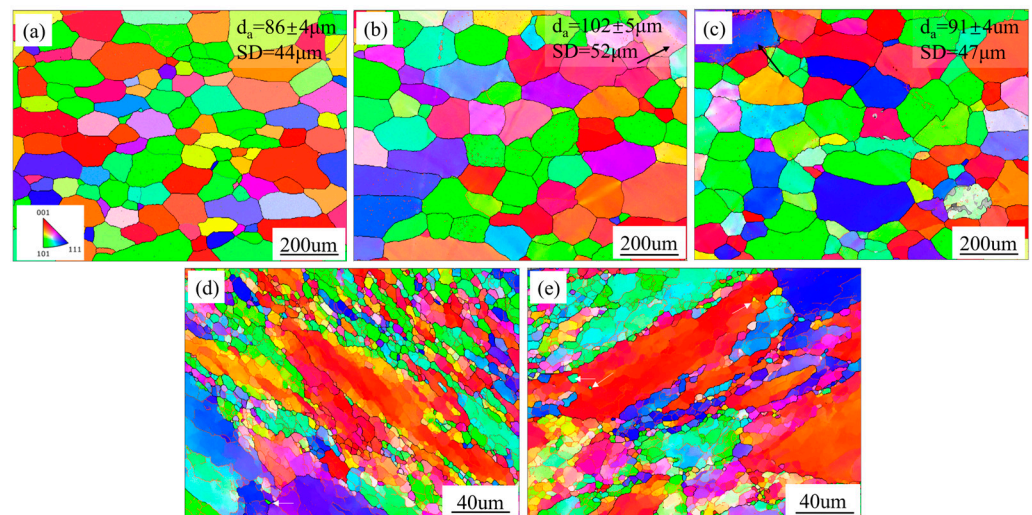
Figure 3. Microstructure of alloy FSW joint at rotation speed of 1250 r/min (**a**) AS, (**b**) NZ, (**c**) RS.


Figure 4. Microstructure of alloy FSW joint at rotation speed of 1500 r/min (**a**) AS, (**b**) NZ, (**c**) RS.

Figures 5–7 show the EBSD characterization and analysis of the different regions of the joint and the BM at a rotational speed of 1000 r/min. The EBSD diagram of HAZ is 5 mm from the exact center of NZ. TMAZ is 2 mm from the center of NZ. The aluminum alloy is rolled into a sheet after T6 heat treatment, and recrystallization occurs. In addition, some grains are elongated along the rolling direction, as shown in Figure 5a. After FSW of the BM, the grains in the HAZ grow significantly under the influence of the welding thermal cycle, with grain growth in the AS-HAZ being more pronounced. Statistically, the average grain growth in the AS-HAZ increases from 85.58 μm to 101 μm in the BM. The grains in the TMAZ are deflected along the direction of shear force under the action of shear extrusion, as shown in Figure 5d,e. The grain organization in the TMAZ is relatively chaotic due to varying temperature and strain gradients [15]. The places far from the stirring pins in the TMAZ are subjected to very small temperatures and strains; thus, very coarse shear bands are generated. Inside these coarse shear bands, there are many grains caused by dislocation slip and strain. There are many low-angle grain boundaries created by dislocation slip and stacking, and most of these low-angle grain boundaries are oriented in the same direction as the shear direction. Closer to the stirring pin, the strain and temperature increase, the proportion of low-angle grain boundaries increases, and the orientation angle increases. However, due to the limited degree of plastic deformation, the grains form inhomogeneous shear bands. Finally, close to the stirring pin, the grains form fine shear bands with a certain aspect ratio under the action of stronger temperature and shear as some dynamic recrystallization occurs. Some of the grains in the HAZ are subjected to shear compression from the grains in the TMAZ. Dynamic restitution occurs under the influence of the weld thermal cycle, producing a number of low-angle grain boundaries (as shown by the black arrows in Figure 5b,c). Conversely, the RS-HAZ is subjected to a relatively high squeezing force, producing additional low-angle grain boundaries; thus, the percentage of high-angle grain boundary length in the base material is higher than that in the HAZ, as shown in Figure 6. As mentioned earlier, the TMAZ produces many low-angle grain boundaries under the effects of temperature and strain, and the percentage of high-angle grain boundary length in the TMAZ is the lowest. Moreover, the high-angle grain boundaries in the AS-TMAZ are greater than those in the RS-TMAZ due to the higher plastic deformation and temperature. These factors lead to the occurrence of dynamic recrystallization to a higher extent in the AS-TMAZ than in the RS-TMAZ.

Figure 5. Microstructure of alloy FSW joint at BM and speed of 1000 r/min (**a**) BM, (**b**) AS-HAZ, (**c**) RS-HAZ, (**d**) AS-TMAZ, (**e**) RS-TMAZ.
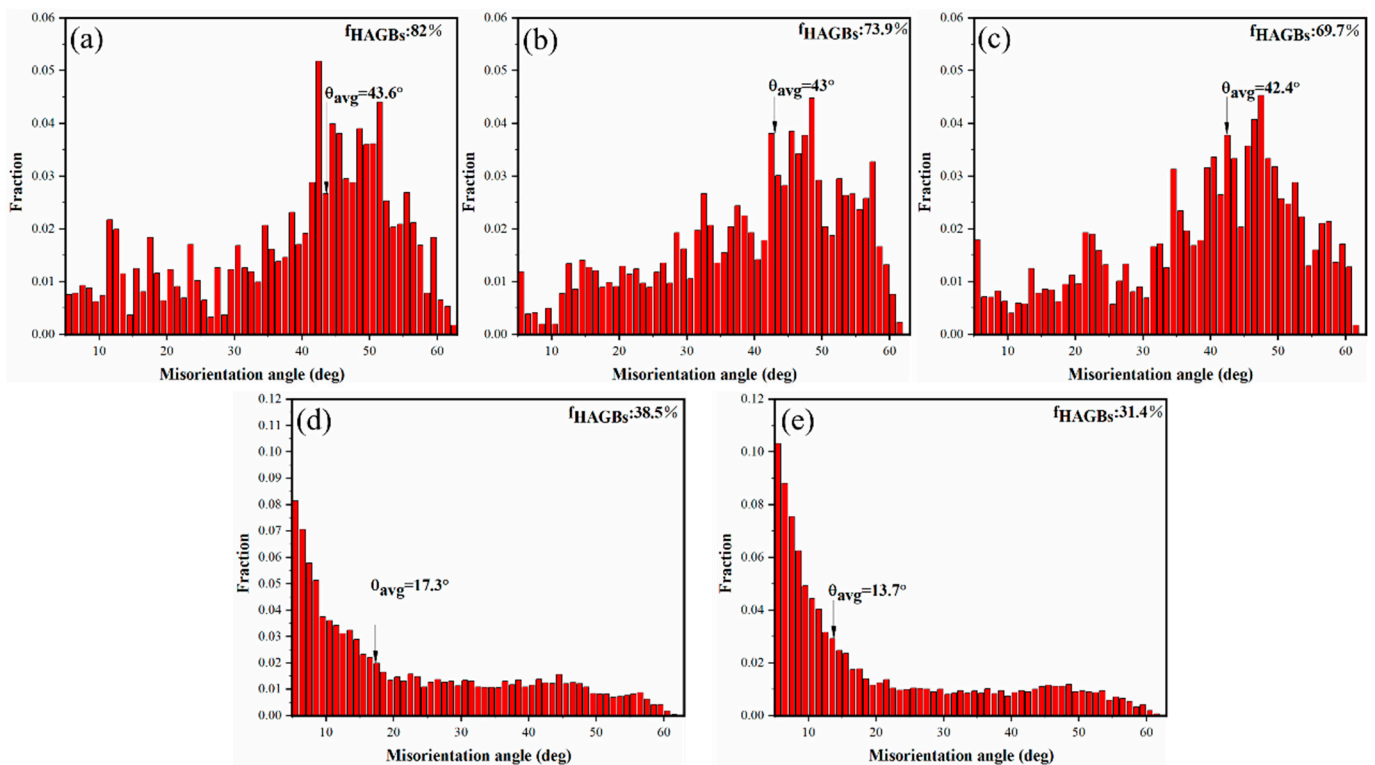
Figure 6. Misorientation distribute maps of the FSW joint at BM and speed of 1000 r/min (**a**) BM, (**b**) AS-HAZ, (**c**) RS-HAZ, (**d**) AS-TMAZ, (**e**) RS-TMAZ.

Grain orientation spread (GOS) is the best technique for distinguishing the degree of grain deformation [16]. It is generally accepted that grains with GOSs of less than 2° are recrystallized grains [17]. TMAZ grains are subjected to large shear extrusion pressure and thermal cycling, which leads to rapid dislocation proliferation and the formation of deformed grains. In the process of dynamic recovery, the deformed grains will transform into subgrains. In addition, the grain near the NZ is subjected to relatively large shear force and thermal cycling, which leads to dynamic recrystallization of a few grains. Therefore, the proportion of recrystallized grains in TMAZ is very low. The plastic deformation on the forward side is higher than that on the backward side, so the capacity for dynamic

recrystallization on the forward side is greater than that on the backward side, resulting in a higher percentage of recrystallized grains in the AS-TMAZ than in the RS-TMAZ.
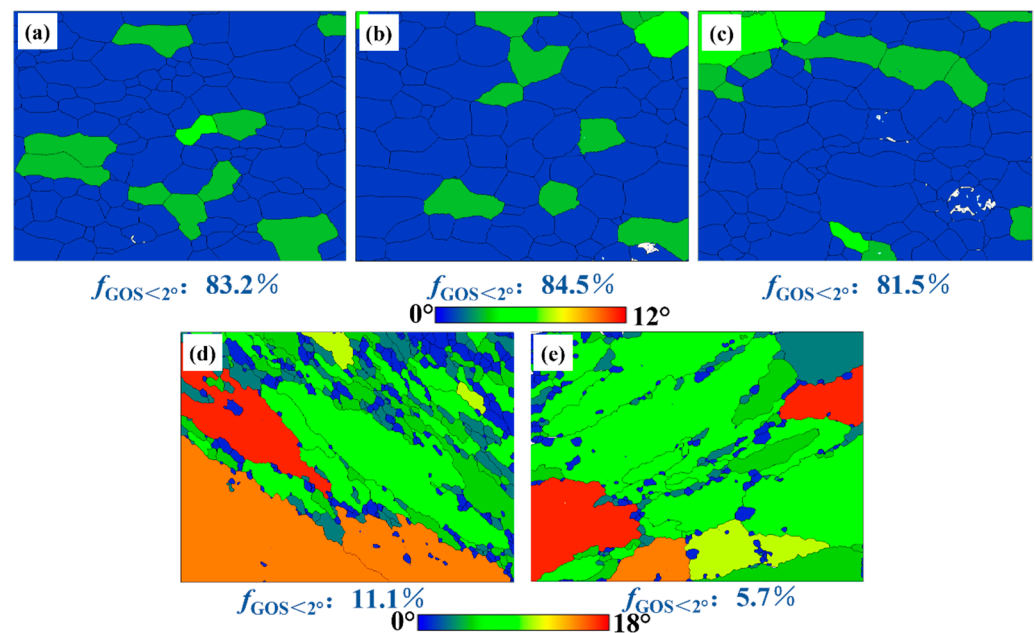
Figure 7. GOS maps of alloy at BM and speed of 1000 r/min (**a**) BM, (**b**) AS-HAZ, (**c**) RS-HAZ, (**d**) AS-TMAZ, (**e**) RS-TMAZ.

The texture is an indication of the orientation of the grains in the alloy material, and the polar diagram is a stereographic projection of the grain orientation and density [18]. Figure 8 shows the polar diagrams of the different areas of the joint and the (100), (110), and (111) directions of the base material at a rotational speed of 1000 r/min. After T6 heat treatment of rolled aluminium alloy plates, the texture components become more complex, retaining the G (110)<100>, B (110)<112>, and S (123)<634> textures generated during rolling but also generating the R-cubeRD (012)<100>, P (110)<211>, and cube (001)<100> recrystallization textures and the C (001)<110> shear texture. The formation of R-cubeRD and P textures may be related to particle-stimulated nucleation (PSN). The texture density in the HAZ is lower than that of the base material, probably because the heat input induces the transition of the rolled texture into a recrystallized texture. Since the grains in the HAZ close to the joint are subjected to less plastic deformation, the HAZ has only one more A(11-1)<1–10> shear texture than the BM. The TMAZ of the joint has approximately the same texture density as the parent material but is subjected to greater shear, making the texture component predominantly shear. The AS-TMAZ of the joint is subjected to a relatively great shear force, mainly forming A and C shear textures. Conversely, the RS-TMAZ of the joint is subjected to less shear force, and A_1^* (11-1)<112> and C shear textures are formed.

The EBSD characterization and analysis of the NZ of the alloy at different stirring head rotation speeds are shown in Figure 9. The presence of serrated grains is shown in Figure 9a,d,g,j. These grains are elongated and divided into segments by low-angle grain boundaries, and a certain amount of Geometric Dynamic Recrystallisation (GDRX) of the NZ grains occurs [15,19]. At 750 r/min, NZ grains produce many serrated crystals under the action of shear force. With the increase in rotational speed, not only do the serrated grains undergo growth, but the number of segments cut by low-angle grain boundaries continues to decrease due to the increased rotational speed improving the heat input and promoting the occurrence of Dynamic Recrystallisation (DRX). Therefore, the serrated crystals produce new DRX grains. Continuous dynamic recrystallization of grains (CDRX) occurs based on a certain degree of GDRX. At the same time, by observing Figure 9i,l,

it can be found that the grain size of NZ does not change significantly with the increase in rotational speed, which indicates that CDRX is conducive to grain refinement. The high-angle grain boundaries and the average orientation deviation angle fractions of the grains in the NZ show a pattern of first decreasing and then increasing with increasing stirrer head rotational speed, as shown in Figure 9b,e,h,k. At a stirrer head rotational speed of 1000 r/min, the average orientation deviation angle of the grains in the NZ is the lowest at 24.2°, while the lowest percentage of NZ high-angle grain boundaries length is 57.6% at a rotation speed of 1250 r/min. The NZ high-angle grain boundaries and the average orientation deviation angle are lower at a rotational speed of 1500 r/min than at 750 r/min. It is clear that the increase in stirring head speed increases the plastic deformation and heat input, leading to more dislocations. Additionally, more low-angle grain boundaries are formed during the dynamic recovery process. Therefore, from 750 r/min to 1250 r/min, the number of low-angle grain boundaries gradually increases. At a rotational speed of 1500 r/min, the average grain size of the NZ is 8.22 μm, as shown in Figure 9l. Compared to 1250 r/min, the grain size of the NZ does not change significantly, which is obviously caused by the enhancement in the ability to generate DRX. This phenomenon results in the production of more recrystallized grains. As a result, the number of high-angle grain boundaries increases. According to the statistics of the recrystallized grains in the weld core region at different rotational speeds, the volume fractions are 41.6%, 41.3%, 37.1%, and 43.6% (As shown in Figure 10) and the highest volume fraction of recrystallization is found at 1500 r/min, which is consistent with the previous analysis.
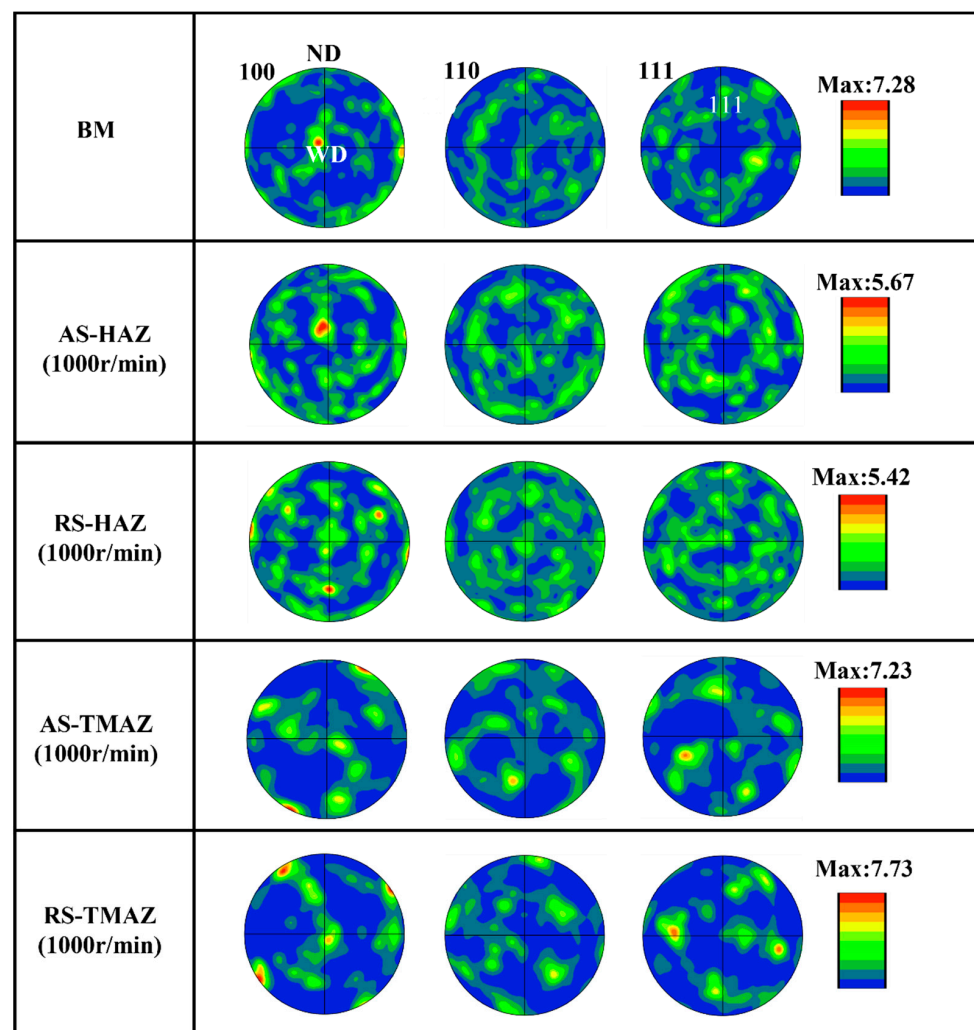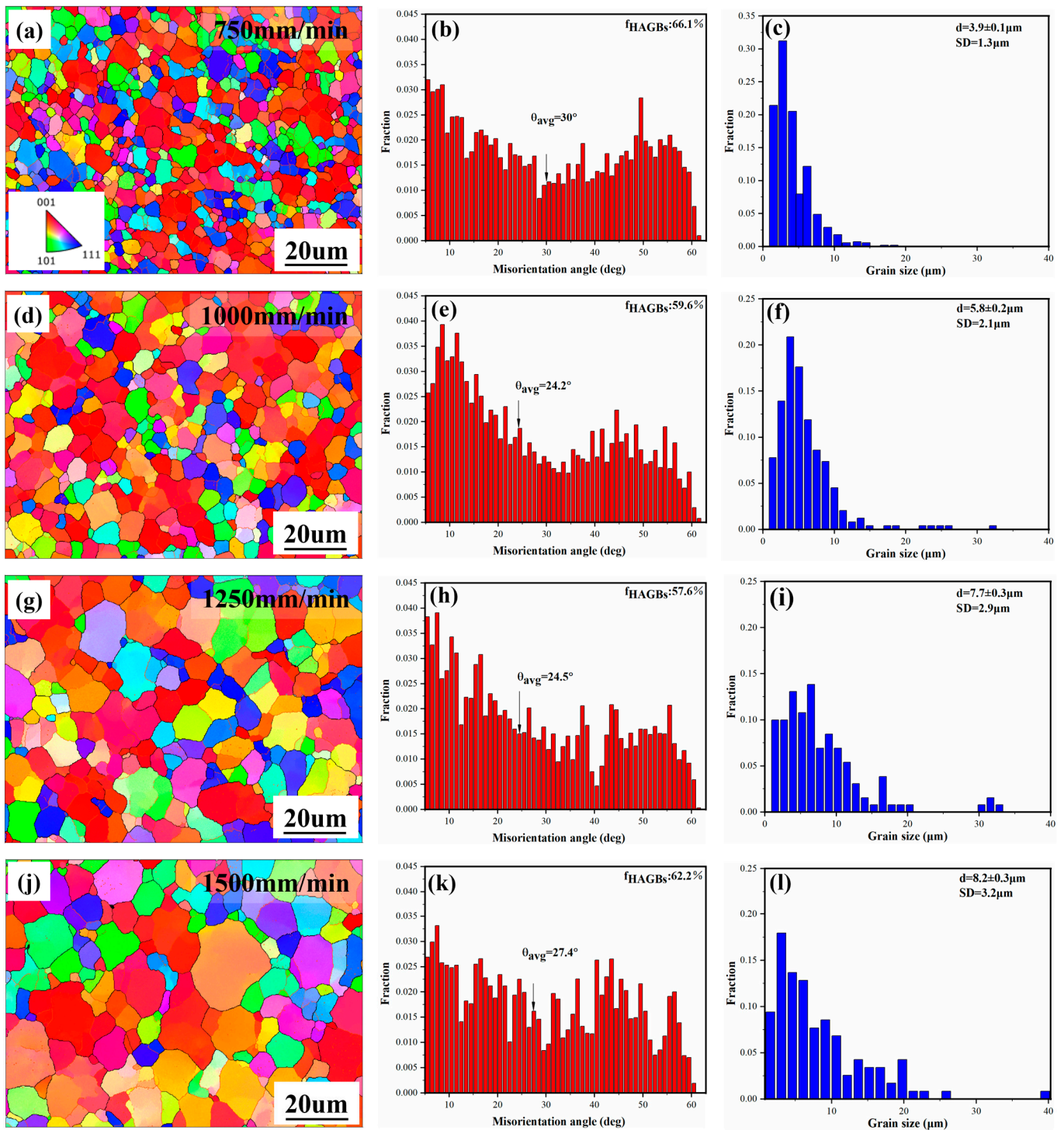

Figure 8. Pole figures of alloy at BM and speed of 1000 r/min.

Figure 9. IPF + GB, misorientation, and grain size distribute maps of the NZs at different rotation speeds: (**a**–**c**) 750 r/min, (**d**–**f**) 1000 r/min, (**g**–**i**) 1250 r/min, (**j**–**l**) 1500 r/min.

　　　The polar patterns of the NZ for different rotation speeds of the alloy are shown in Figure 11. The texture orientation of the NZ obtained in Figure 11 deviates from the ideal state due to the complex constraints of the FSW process. At a rotational speed of 750 r/min, a large number of C{001}<1−10> textures and a small number of A{11-1}<1−10> textures mainly exist in the weld core region. With the increase in rotational speed, at 1000 r/min, the texture density of the C texture increases while the A texture disappears, and a new B{11-2}<1−10> texture is produced with a very low texture density. At 1250 r/min and

1500 r/min, the density of the C texture begins to decrease but remains the dominant texture component in the weld core region. Conversely, the density of the B texture increases slightly. The reasonable explanation for this phenomenon is that in the process of plastic deformation, the aluminum alloy {111} slip plane is in line with the shear face, and the <110> slip direction is parallel to the shear direction. Therefore, it is easy to produce $A/\overline{A}$ texture under shearing force [20]. With the increase in shear force, the {112} slip plane will activate, thus forming the $B/\overline{B}$ texture [21,22]. The understanding of shear textural evolution is provided in some experimental and theoretical studies of FCC metals [23–26]. However, in these experiments, the C texture is dominant, and the texture density is low despite the appearance of the B texture. Since dynamic recrystallization occurs in NZ grains, the type of NZ texture identified in some studies [27,28] is a cube recrystallization texture. The C texture may be formed by the rotational squeezing force of the cube texture by the axial shoulder [29,30].
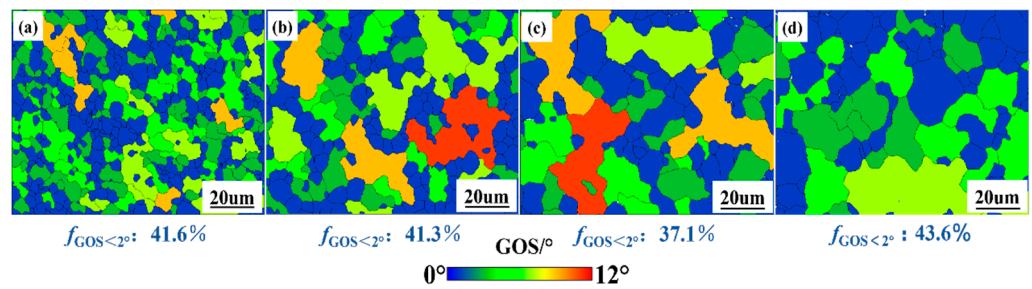

Figure 10. IPF + GB, misorientation, and grain size distribute maps of the NZs at different rotation speeds: (**a**) 750 r/min, (**b**) 1000 r/min, (**c**) 1250 r/min, (**d**) 1500 r/min.
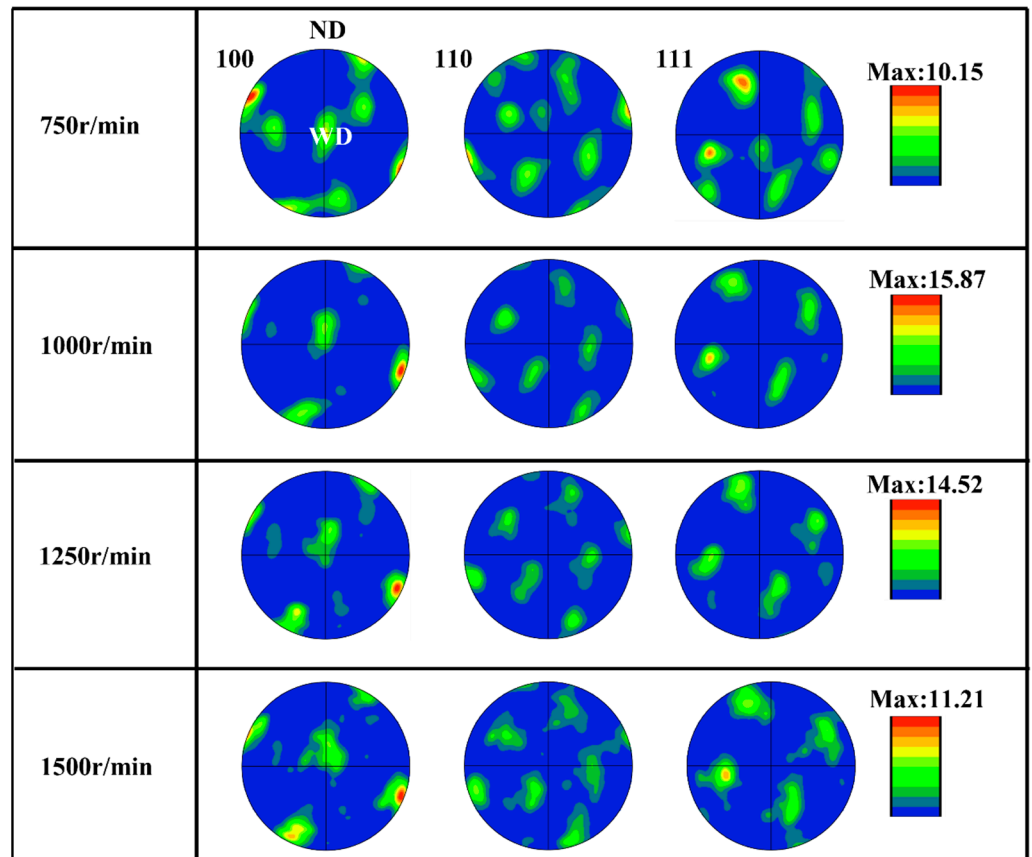

Figure 11. Pole figures of the NZs at different rotation speeds.

3.2. Mechanical Properties

The hardness distribution curve at the center of the cross-section of the FSW joint is shown in Figure 12. The hardness curve of the joint shows a W-shape. During the FSW process, the β'' phase in the NZ is dissolved, and overaged precipitated phases, such as β' and Q', are generated. The increase in the tool rotational speed induces these overaged phases to break up and dissolve, while the residual heat after stirring produces a transient aging effect, which causes clusters of solute atoms to precipitate and grow [9,31]. By comparing Figure 12a,b, it can be found that the hardness of NZ increases significantly at 1000 r/min. With the continuous increase of rotational speed, the hardness of NZ does not change much when the error is considered, which may be caused by the joint action of grain size and short aging after welding. At low rotational speeds, the TMAZ and HAZ hardnesses are approximately the same. At high speeds, the hardness of the TMAZ is almost the same as that of the NZ, which may be due to the increase in dislocation density caused by the increase in rotational speed. The HAZ has a low dislocation density, overaged phase coarsening, and grain growth; thus, the hardness of the HAZ is the lowest in the joint. Moreover, the hardness of the AS-HAZ is lower than that of the RS-HAZ due to the pronounced grain size growth.
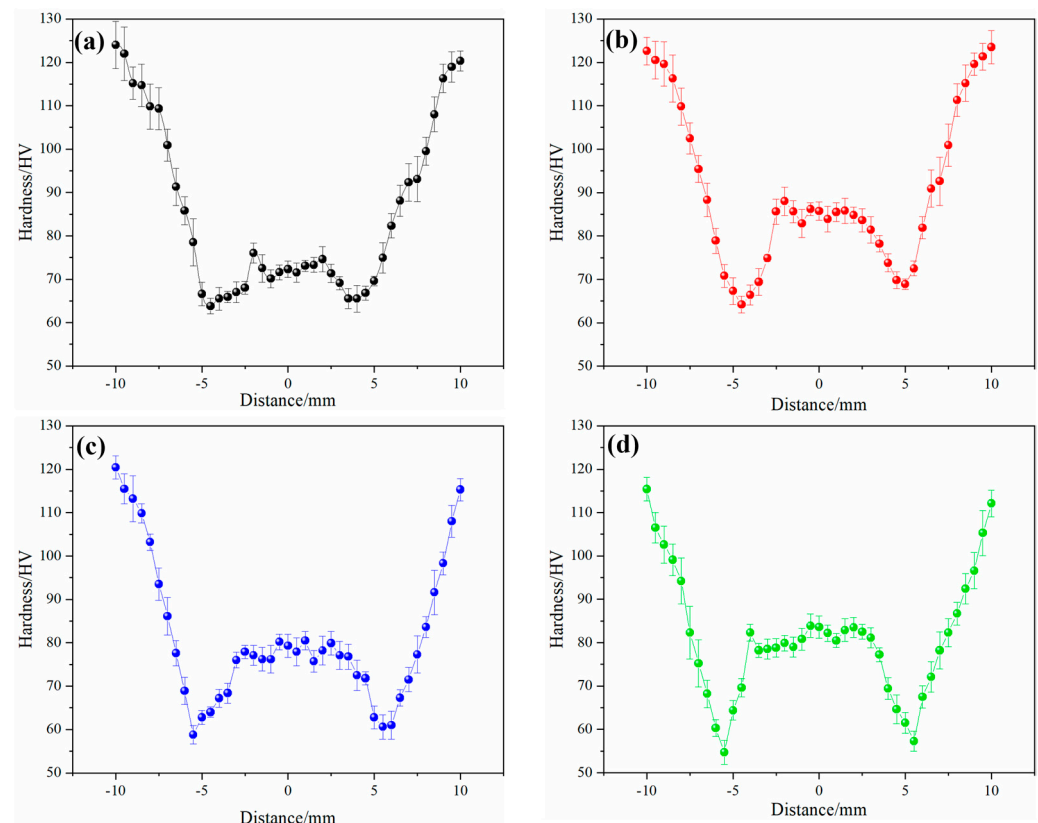

Figure 12. Microhardness curves at different rotation speeds: (**a**) 750 r/min, (**b**) 1000 r/min, (**c**) 1250 r/min, (**d**) 1500 r/min.

The tensile properties of the BM and different welded specimens are shown in Figure 13, and the specific values are given in Table 1. First, the tensile properties of the specimens after FSW decrease drastically due to the dissolution and coarsening of precipitated phases during the thermal cycling of the joint. Second, the UTS first increases and then decreases with increasing rotational speed, while the elongation decreases with increasing rotational speed. The performance of the joints is generally highly related to the hardness. In Figure 12, the highest value of NZ hardness is found at a rotational speed of 1000 r/min, and the lowest value of hardness is approximately the same at 750 r/min and

1000 r/min. At high rotational speeds, a significant decrease in the hardness of the HAZ occurs. In addition, the dissolution of the joint precipitation phase leads to the softening of the joint, improving the plasticity of the alloy. However, with increasing rotational speed, the overaged phase in the HAZ gathers and coarsens, leading to a significant decrease in the properties of the alloy. Thus, at low rotational speeds, the elongation is higher than that of the base material, and with increasing rotational speed, the elongation gradually decreases. At a rotational speed of 750 r/min, the elongation of the joint is higher than that of the base material. At a rotational speed of 1000 r/min, the joint has the highest tensile strength and higher elongation than the parent material, but the joint efficiency is only 61.25% of that of the parent material. In combination with Figure 12, it can be seen that the whole joint undergoes different degrees of softening under different temperature conditions, which indicates that the dissolution and coarsening of the precipitated phase leads to the loss of joint strength. Additionally, all the welded specimens show significant jagged curves during tensile testing, as shown in Figure 13b. Baghdadi [32] believes that this phenomenon occurs due to the uneven distribution of hard particles (Mg_2Si) in the alloy. Due to the obvious temperature gradient in each area of the joint, the degree of dissolution and coarsening of precipitates in different areas is different, resulting in an uneven distribution of precipitates in each area, resulting in the PLC effect.
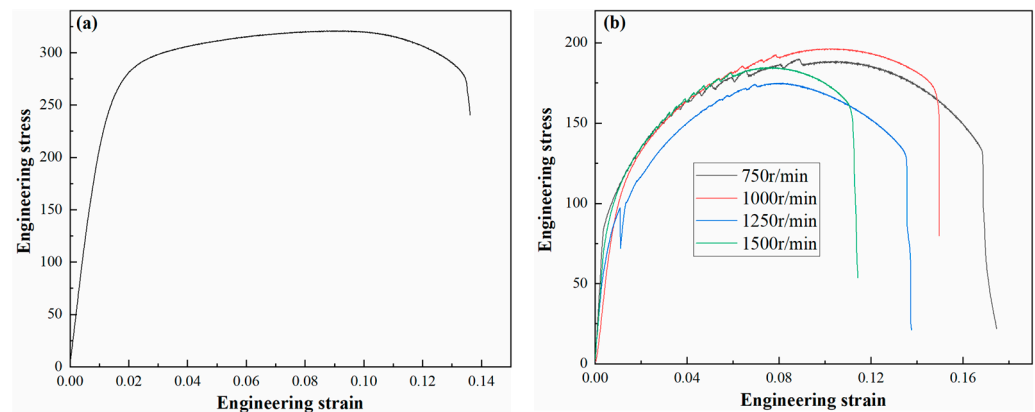

Figure 13. Tensile properties of joints at different welding speeds: (**a**) BM, (**b**) joint.

Table 1. Transverse tensile properties of BM and FSW joints.

| Part	Rotational Speeds/(r/Min)	UTS/MPa	Elongation/%
BM	-	320 ± 4	12.6 ± 1.2
	750	185 ± 1	15.9 ± 0.7
	1000	196 ± 3	13.5 ± 0.9
FSW joint	1250	175 ± 2	9.9 ± 1.4
	1500	186 ± 1	8.2 ± 0.8

Figure 14 shows the fracture location of the joint at different rotational speeds. At 750 r/min and 1000 r/min, the fracture location is on the backward side of the joint. However, at 750 r/min, the crack extends along the direction 45° from the tensile axis, and the final fracture location is at the top of the NZ towards the edge of the receding side. This phenomenon occurs due to the complex transformation of the microstructure near the interface between the TMAZ and NZ, resulting in the appearance of low Taylor index grain bands in this region and forming a local crystallographic weak zone, leading to the fracture of the crack after its formation through this weak zone [33,34]. At 1000 r/min, the fracture direction of the crack is opposite to that at 750 r/min, and the fracture region tends to be between the RS-HAZ and RS-TMAZ. This region may be generated due to the low dislocation density and serious microstructural inhomogeneity, as shown in Figure 5e. At 1250 and 1500 r/min, the joints fracture in the position of the AS-HAZ, which is attributed

to the overaging phase of overaged phase aggregation and coarsening, leading to easy cracking in this region.
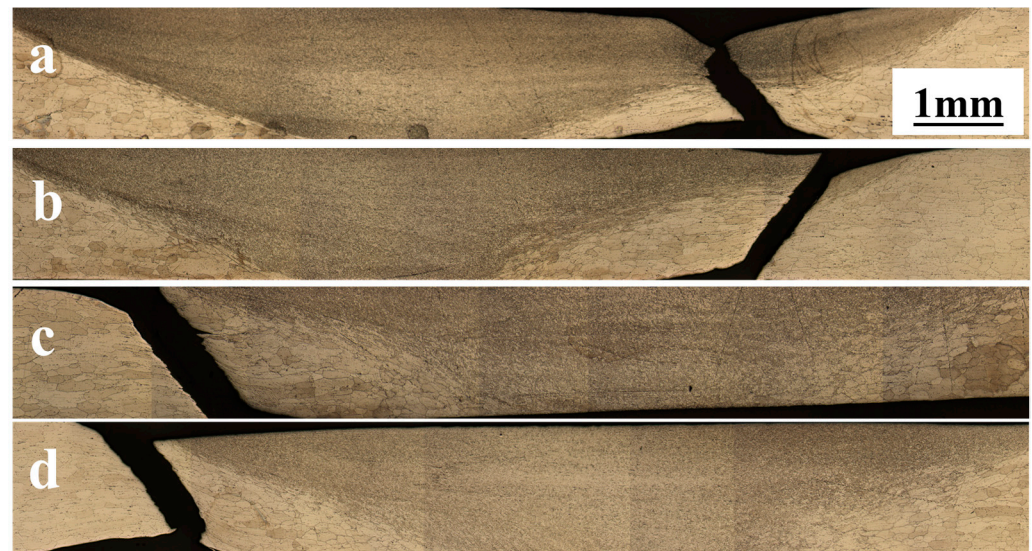
Figure 14. Tensile fracture morphology of samples at different welding speeds: (**a**) 750 r/min, (**b**) 1000 r/min, (**c**) 1250 r/min, (**d**) 1500 r/min.

Figure 15 shows SEM photographs of the fracture of the joint at different rotational speeds. From the figure, it can be seen that both the parent material and the joint undergo ductile fractures. In this case, the tensile fracture of the parent material has both large and small dimples, and there are second-phase particles inside the dimples, making the parent material moderately tough. At 750 r/min, the morphology of the tensile fracture shows the presence of small and dense dimples, and its elongation is highest in this process. At 1000 r/min, there are some large and small dimples, but they are shallow. At higher speeds, the tensile fracture shows a convoluted surface, indicating that the toughness of the joint is poor.
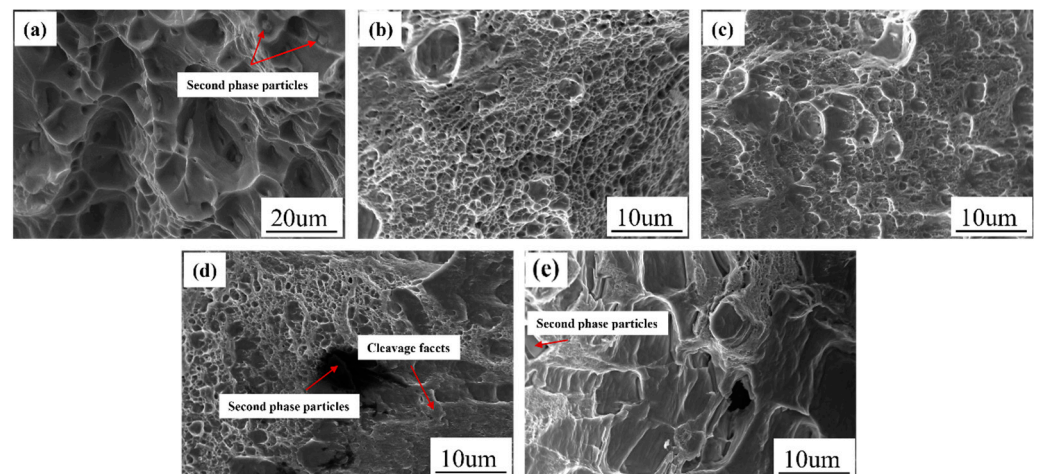
Figure 15. SEM tensile fracture images of BM and FSW joints: (**a**) BM, (**b**) 750 r/min, (**c**) 1000 r/min, (**d**) 1250 r/min, (**e**) 1500 r/min.

4. Conclusions

(1) During the friction stir welding process, the grains of the heat-affected zone are slightly larger than those of the base metal. The thermomechanically affected zone undergoes partial dynamic recrystallization, resulting in an extremely heterogeneous

structure due to the temperature and strain gradients. The base metal mainly consists of rolled and recrystallized textures. The texture density of the heat-affected zone is weaker than that of the base material, and the heat-affected zone has more A-texture. The thermal mechanically affected zone has a shear texture because it is subjected to shear forces. Among them, the advancing side of the thermomechanically affected zone has A and C shear textures, and the receding side of the thermomechanically affected zone has A_1^* and C shear textures.

(2) During the friction stir welding process, the nugget zone structure experiences thermo-mechanical coupling, resulting in geometric dynamic recrystallization and continuous dynamic recrystallization. With increasing rotational speed, the nugget zone grain size gradually increases. Additionally, the percentage of low-angle grain boundaries first increases and then decreases. Finally, the type of texture is gradually converted from A and C to B and C, with the C texture being the primary component of the nugget zone.

(3) With increasing rotational speed, the tensile strength of the AlMgSiCu alloy welded joints first increases and then decreases while the elongation decreases. The optimum performance of the joints is obtained at a rotational speed of 1000 r/min, with tensile strength and elongation of 196 MPa and 13.5%, respectively. Due to the precipitation dissolution and coarsening in different areas of the joint, the strength efficiency of the joint is only 61.25% of that of the base material under the optimal process. The fracture form of the AlMgSiCu alloy joints is ductile fracture.

Abbreviations

FSW	Friction stir welding
TMAZ	Thermal-mechanically affected zone
BM	Base metal
GDRX	Geometric Dynamic Recrystallization
HAZ	Heat affected zone
CDRX	Continuous Dynamic Recrystallization
NZ	Nugget zone
EBSD	Electron back-scattering Patterns
AS	Advancing side
RS	Receding side

References

1. Meng, X.; Huang, Y.; Cao, J.; Shen, J.; Santos, J.F.D. Recent progress on control strategies for inherent issues in friction stir welding. *Prog. Mater. Sci.* **2021**, *115*, 100706. [CrossRef]
2. Mishra, R.S.; Ma, Z.Y. Friction stir welding and processing. *Mater. Sci. Eng. R. Rep.* **2005**, *50*, 1–78. [CrossRef]

3. Wang, G.; Zhao, Y.; Hao, Y. Friction stir welding of high-strength aerospace aluminum alloy and application in rocket tank manufacturing. *J. Mater. Sci. Technol.* **2017**, *34*, 73–91. [CrossRef]

4. Liu, H.J.; Hou, J.C.; Guo, H. Effect of WS on Microstructure and mechanical properties of self-reacting friction stir welded 6061–T6 aluminum alloy. *Mater. Des.* **2013**, *50*, 872–878. [CrossRef]

5. Mosleh, A.O.; Yakovtseva, O.A.; Kishchik, A.A.; Kotov, A.D.; Moustafa, E.B.; Mikhaylovskaya, A.V. Effect of Coarse Eutectic-Originated Particles on the Microstructure and Properties of the Friction Stir-Processed Al-Mg-Zr-Sc-Based Alloys. *J. Miner. Met. Mater. Soc.* **2023**, *75*, 2989–3000. [CrossRef]

6. Buffa, G.; Hua, J.; Shivpuri, R.; Fratini, L. Design of the friction stir welding tool using the continuum based FEM model. *Mater. Sci. Eng. A* **2006**, *419*, 381–388. [CrossRef]

7. Dong, P.; Li, H.; Sun, D.; Gong, W.; Liu, J. Effects of welding speed on the microstructure and hardness in friction stir welding joints of 6005A-T6 aluminum alloy. *Mater. Des.* **2013**, *45*, 524–531. [CrossRef]

8. Krasnowski, K.; Hamilton, C.; Dymek, S. Influence of the tool shape and weld configuration on microstructure and mechanical properties of the Al 6082 alloy FSW joints. *Arch. Civ. Mech. Eng.* **2014**, *15*, 133–141. [CrossRef]

9. Sato, Y.S.; Urata, M.; Kokawa, H. Parameters controlling microstructure and hardness during friction-stir welding of precipitation-hardenable aluminum alloy 6063. *Metall. Mater. Trans. A* **2002**, *33*, 625–635. [CrossRef]

10. Fauzi, M.A.; Uday, M.B.; Zuhailawati, H.; Ismail, A.B. Microstructure and mechanicalproperties of alumina-6061 aluminum alloy joined by friction welding. *Mater. Des.* **2010**, *31*, 670–676. [CrossRef]

11. Li, H.; Wang, X.L.; Shi, Z.X.; Wang, Z.X.; Zheng, Z.Q. Precipitation behaviors of Al-Mg-Si-(Cu) aluminum alloys during continuous heating. *Chin. J. Nonferrous Metals.* **2011**, *21*, 2028–2034.

12. Wang, Z.X.; Li, H.; Gu, J.H.; Song, R.G.; Zheng, Z.J. Effect of Cu content on microstructures and properties of Al-Mg-Si-Cu alloy. *Chin. J. Nonferrous Met.* **2012**, *22*, 3348–3355. [CrossRef]

13. Chen, Y.; Wei, W.; Zhao, Y.; Shi, W.; Zhou, X.; Rong, L.; Wen, S.; Wu, X.; Gao, K.; Huang, H.; et al. Effect of solid solution and aging treatment on microstructure and mechanical properties of Al-Mg-Si-Cu alloy. *Trans. Mater. Heat Treat.* **2017**, *38*, 30–37. [CrossRef]

14. Liu, H.; Hu, Y.; Dou, C.; Sekulic, D.P. An effect of the rotation speed on microstructure and mechanical properties of the friction stir welded 2060-T8 Al-Li alloy. *Mater. Charact.* **2017**, *123*, 9–19. [CrossRef]

15. Prangnell, P.B.; Heason, C.P. Grain structure formation during friction stir welding observed by the 'stop action technique'. *Acta Mater.* **2005**, *53*, 3179–3192. [CrossRef]

16. Peng, Y.; Huang, B.; Zhong, Y.; Su, C.; Tao, Z.; Rong, X.; Li, Z.; Tang, H. Electrochemical corrosion behavior of 6061 Al alloy under high rotating speed submerged friction stir processing. *Corros. Sci.* **2023**, *215*, 111029. [CrossRef]

17. Field, D.P.; Bradford, L.T.; Nowell, M.M.; Lillo, T.M. The role of annealing twins during recrystallization of Cu. *Acta Mater* **2007**, *55*, 4233–4241. [CrossRef]

18. Shi, L.; Dai, X.; Tian, C.; Wu, C. Effect of splat cooling on microstructures and mechanical properties of friction stir welded 2195 Al–Li alloy. *Mater. Sci. Eng. A* **2022**, *858*, 144169. [CrossRef]

19. Wang, T.; Zou, Y.; Matsuda, K. Micro-structure and micro-textural studies of friction stir welded AA6061-T6 subjected to different rotation speeds. *Mater. Des.* **2016**, *90*, 13–21. [CrossRef]

20. Fonda, R.W.; Bingert, J.F. Texture variations in an aluminum friction stir weld. *Scr. Mater.* **2007**, *57*, 1052–1055. [CrossRef]

21. Sidor, J.J.; Petrov, R.H.; Kestens, L.A.I. Modeling the crystallographic texturechanges in aluminum alloys during recrystallization. *Acta Mater.* **2011**, *59*, 5735–5748. [CrossRef]

22. Bo, W.; Dan-Qing, Y.; Yu-Qiang, C.; Bin, W.; Zeying, L. Evolution of texture and microstructure of 2E12 aluminum alloy during cold rolling and annealing. *Chin. J. Nonferrous Met.* **2013**, *23*, 3064–3074. [CrossRef]

23. Canova, G.R.; Kocks, U.F.; Jonas, J.J. Theory of torsion texture development. *Acta Metall.* **1984**, *32*, 211–226. [CrossRef]

24. Barnett, M.R.; Montheillet, F. The generation of new high-angle boundaries in aluminium during hot torsion. *Acta Mater.* **2002**, *50*, 2285–2296. [CrossRef]

25. Toth, L.S.; Gilormini, P.; Jonas, J.J. Effect of rate sensitivity on the stability of torsion textures. *Acta Metall.* **1988**, *36*, 3077–3091. [CrossRef]

26. Yuqi, L.; Tianliang, L.; Zhong, L.; Chuanmei, W.; Zhimin, Z.; Long, J.; Bing, L. Numerical and experimental investigations on dynamic behaviors of a bolted joint rotor system with pedestal looseness. *J. Sound Vib.* **2024**, *571*, 118036.

27. Suhuddin, U.F.H.R.; Mironov, S.; Sato, Y.S.; Kokawa, H.J.M.S. Grain structure and texture evolution during friction stir welding of thin 6016 aluminum alloy sheets. *Mater. Sci. Eng. A* **2010**, *527*, 1962–1969. [CrossRef]

28. Chen, S.; Jiang, X. Texture evolution and deformation mechanism in friction stir welding of 2219Al. *Mater. Sci. Eng. A* **2014**, *612*, 267–277. [CrossRef]

29. Zhang, L.; Wang, X.; Wei, X. Evolution of Grain Structure and Texture for 6082-T6 Aluminum Alloy during Friction Stir Welding. *J. Wuhan Univ. Technol. Mater. Sci. Ed.* **2019**, *34*, 397–403. [CrossRef]

30. Luo, Z.; Sun, Y.; Li, W.; He, J.; Luo, G.; Liu, H. Evolution of Microstuctures, texture and Mechanical Properties of Al-Mg-SiCu Alloy under Difffierent Welding Speedsduring Friction Stir Welding. *Metals* **2023**, *13*, 1120. [CrossRef]

31. Tao, W.; Yong, Z.; Xuemei, L.; Matsuda, K. Special grain boundaries in the nugget zone of friction stir welded AA6061-T6 under various welding parameters. *Mater. Sci. Eng. A* **2016**, *671*, 7–16. [CrossRef]

32. Baghdadi, A.H.; Rajabi, A.; Selamat, N.F.M.; Sajuri, Z.; Omar, M.Z. Effect of post-weld heat treatment on the mechanical behavior and dislocation density of friction stir welded Al6061. *Mater. Sci. Eng. A* **2019**, *754*, 728–734. [CrossRef]

33. Tao, Y.; Ni, D.R.; Xiao, B.L.; Ma, Z.Y.; Wu, W.; Zhang, R.X.; Zeng, Y.S. Origin of unusual fracture in stirred zone for friction stir welded 2198-T8 Al-Li alloy joints. *Mater. Sci. Eng. A* **2017**, *693*, 1–13. [CrossRef]
34. Zhang, Z.; Wei, S.; Wang, P.; Qiu, W.; Zhang, G. Progress in applications of laser induced cavitation on surface processing. *Opt. Laser Technol.* **2024**, *170*, 110212. [CrossRef]